Chem

CellPress
OPEN ACCESS

Article

Sculpting DNA-based synthetic cells through phase separation and phase-targeted activity

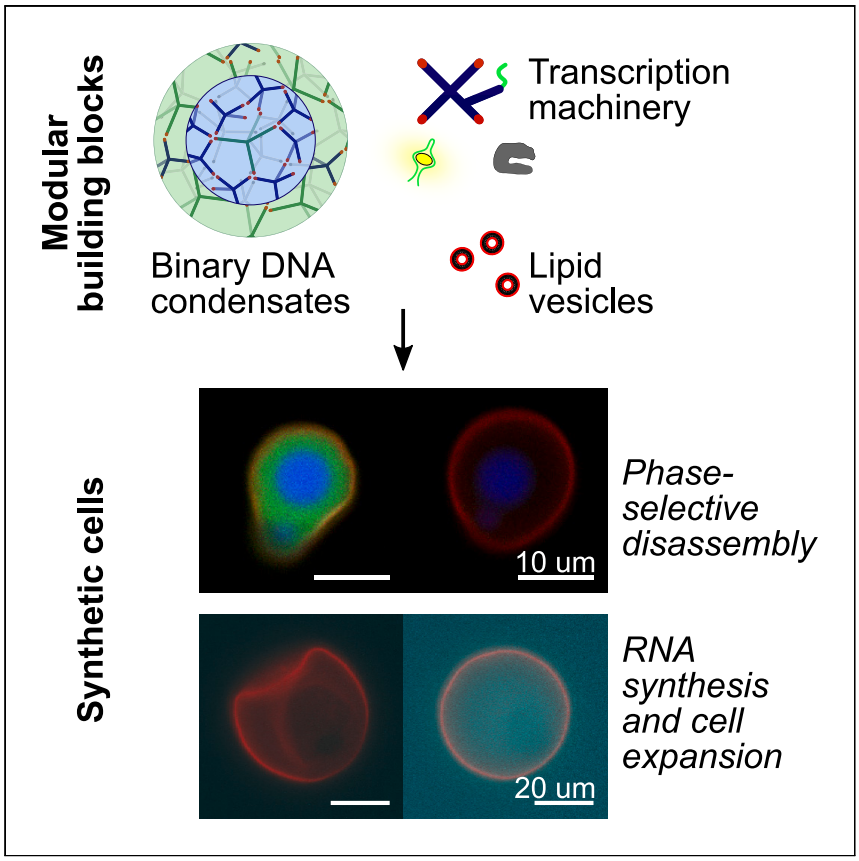

Mixtures of amphiphilic DNA constructs robustly self-assemble into condensates with multiple compartments. By combining these complex synthetic condensates with other modular building blocks, including transcription machinery and lipid membranes, we construct synthetic cells with features akin to eukaryotic cells. These synthetic cells localize distinct processes in different sub-compartments and support life-like functions. Our strategy could be exploited for the rational design of cell mimics with physically distinct and chemically addressable microenvironments, with potential applications including biosensing and drug delivery.

Layla Malouf, Diana A. Tanase, Giacomo Fabrini, ..., Adrian Leathers, Michael J. Booth, Lorenzo Di Michele

ld389@cam.ac.uk

Highlights

DNA self-assembly and phase separation produce multi-phase condensates

Design rules prescribe condensate phase behavior and microstructure

Protein and lipid building blocks are included to produce synthetic cells

Phase-specific responses and biochemical activity produce life-like responses

Malouf et al., Chem 9, 3347–3364
November 9, 2023
Published by Elsevier Inc.
https://doi.org/10.1016/j.chempr.2023.10.004

Chem

CellPress
OPEN ACCESS

Article

Sculpting DNA-based synthetic cells through phase separation and phase-targeted activity

Layla Malouf,[1,2] Diana A. Tanase,[1,2] Giacomo Fabrini,[2] Ryan A. Brady,[3] Miguel Paez-Perez,[2] Adrian Leathers,[4] Michael J. Booth,[5] and Lorenzo Di Michele[1,2,6,7,*]

SUMMARY

Synthetic cells, like their biological counterparts, require internal compartments with distinct chemical and physical properties where different functionalities can be localized. Inspired by membrane-less compartmentalization in biological cells, here, we demonstrate how microphase separation can be used to engineer heterogeneous cell-like architectures with programmable morphology and compartment-targeted activity. The synthetic cells self-assemble from amphiphilic DNA nanostructures, producing core-shell condensates due to size-induced de-mixing. Lipid deposition and phase-selective etching are then used to generate a porous pseudo-membrane, a cytoplasm analog, and membrane-less organelles. The synthetic cells can sustain RNA synthesis via *in vitro* transcription, leading to cytoplasm and pseudo-membrane expansion caused by an accumulation of the transcript. Our approach exemplifies how architectural and functional complexity can emerge from a limited number of distinct building blocks, if molecular-scale programmability, emergent biophysical phenomena, and biochemical activity are coupled to mimic those observed in live cells.

INTRODUCTION

Although there is no agreed definition of cellular life,[1] there is general consensus on the fundamental characteristics of living cells, which includes information processing, adaptability, growth and division, metabolism, and compartmentalization.[2,3] Bottom-up synthetic biology aims to create synthetic cells featuring a subset, or all, of these fundamental characteristics by combining elementary molecular building blocks.[2,4] This radical approach, although regarded as more challenging compared with traditional top-down cell engineering, circumvents the complexities inherent to working with and modifying living cells.[1,5] A particularly challenging aspect of synthetic-cell engineering is the production of sufficiently complex and robust cell-like architectures, containing multiple compartments that serve to localize, segregate, and regulate function and environment.[6,7] These enclosures are often membrane-based, constructed from phospholipids and/or fatty acid vesicles,[8–12] polymersomes,[13,14] or proteinosomes,[15,16] but alternative membrane-less architectures are emerging in the form of hydrogel capsules, coacervates, or synthetic condensates.[17–22]

Microfluidics is a typical strategy for producing synthetic-cell scaffolds, being particularly effective at generating monodisperse and nested structures in small quantities.[23] However, the microfluidic approach can be difficult to implement and scale,

THE BIGGER PICTURE

Cells have developed strategies to efficiently organize their molecular components into organelles, both membrane-bound and membrane-less, enabling them to sustain advanced responses by spatially organizing biochemical activity. Designing containers that replicate the multi-compartment architectures of biological cells is a vital step toward the ambitious goal of constructing synthetic cells—devices that mimic cellular structure and functions. These would be highly valuable for therapeutic applications and as models to unravel the rules of life. We apply molecular programming and the physical principles of self-assembly and phase separation to build synthetic cells primarily composed of DNA nanostructures, featuring a membrane, a cytoplasm, and organelles. Similar to biological cells, the DNA-based synthetic cells localize distinct processes in different sub-compartments and support life-like functions, including RNA synthesis, growth, and a disassembly response analogous to cell death.

requiring bespoke, often complex chips and specialized equipment.[24] Similar to bulk emulsification approaches, microfluidics often rely on water-oil mixtures to assemble stabilized droplets or giant vesicles, which adds challenges and steps in the workflow associated with handling and removal of the non-aqueous phase.[25–34] It may instead be more desirable to use techniques that exploit simple physical principles, such as phase separation and self-assembly, while avoiding the use of specialized equipment and non-aqueous components altogether.

The low costs of DNA oligonucleotides,[35] in conjunction with the predictable thermodynamics and kinetics of their interactions,[36,37] and the availability of computational design tools,[38,39] makes DNA nanotechnology[37,40,41] highly attractive to engineer advanced biomimetic devices, including synthetic cells. The latter are often formed from the programmable condensation of DNA building blocks in aqueous environments, hence removing the complexities of microfluidics, emulsification, and other chemical manufacturing routes. Artful examples of DNA-based, cell-like devices have been reported, self-assembled from multiblock single-stranded DNA (ssDNA)[42,43] or from branched DNA junctions known as nanostars.[18–20,44–47] Among condensate-forming DNA motifs, amphiphilic nanostructures, obtained by labeling DNA junctions with hydrophobic moieties, have shown significant potential owing to the stability of the self-assembled phases, their programmable nanostructure, and the possibility of engineering localized functionality and response to various environmental stimuli.[48–51]

Although DNA-based synthetic-cell implementations hold substantial promise due to their facile preparation, robustness, and algorithmic programmability, routes toward generating architectures with sufficiently complex internal structure, akin to those achievable with microfluidic methods, are lacking. In this work, we take advantage of the programmable phase behavior of amphiphilic DNA nanostructures alongside their ability to host stimuli-responsive elements and sustain enzymatic pathways,[50,52–54] to construct cell-like devices that display a complex internal architecture and spatially resolved activity. The DNA-based synthetic cells feature a porous lipid shell as a pseudo-membrane and internal membrane-less organelles. These organelles can be engineered to exhibit different functionalities, from selective etching, which creates a cytoplasm-like space within the lipid shell, to hosting the *in situ* transcription of RNA aptamers by a polymerase, which also induces spatially localized morphological changes to the synthetic cells. Our results demonstrate that the synergy between biophysical and biochemical responses can produce structural and functional complexity akin to that observed in live cells, even in minimalist systems composed of a small number of molecular building blocks.

RESULTS

Generating internal heterogeneity in DNA condensates with phase separation

Our synthetic cells are primarily constructed from C-stars—DNA junctions made amphiphilic through the addition of cholesterol moieties. As sketched in Figure 1Ai, each C-star comprises four identical cholesterol-modified oligonucleotides, designed to hybridize to non-cholesterolized "core" strands that form the central junction. One-pot thermal annealing of stoichiometric mixtures of these strands leads to the formation of polyhedral crystalline aggregates of C-stars[52,53] or spherical, cell-size condensates, as shown in Figure 1Bi.[52] The latter, despite their macroscopic appearance, can be either crystalline or amorphous.[50,52] Aggregate morphology (whether polyhedral or spherical) and the degree of crystallinity have been found to depend on C-star design features, such as size, junction flexibility, quenching

[1]Department of Chemical Engineering and Biotechnology, University of Cambridge, Cambridge CB3 0AS, UK

[2]Department of Chemistry, Imperial College London, London W12 7TA, UK

[3]Department of Structural Biology, St. Jude Children's Research Hospital, Memphis, TN, USA

[4]Cavendish Laboratory, University of Cambridge, Cambridge CB3 0HE, UK

[5]Department of Chemistry, University College London, London WC1H 0AJ, UK

[6]fabriCELL, Imperial College London, London, UK

[7]Lead contact

*Correspondence: ld389@cam.ac.uk

https://doi.org/10.1016/j.chempr.2023.10.004

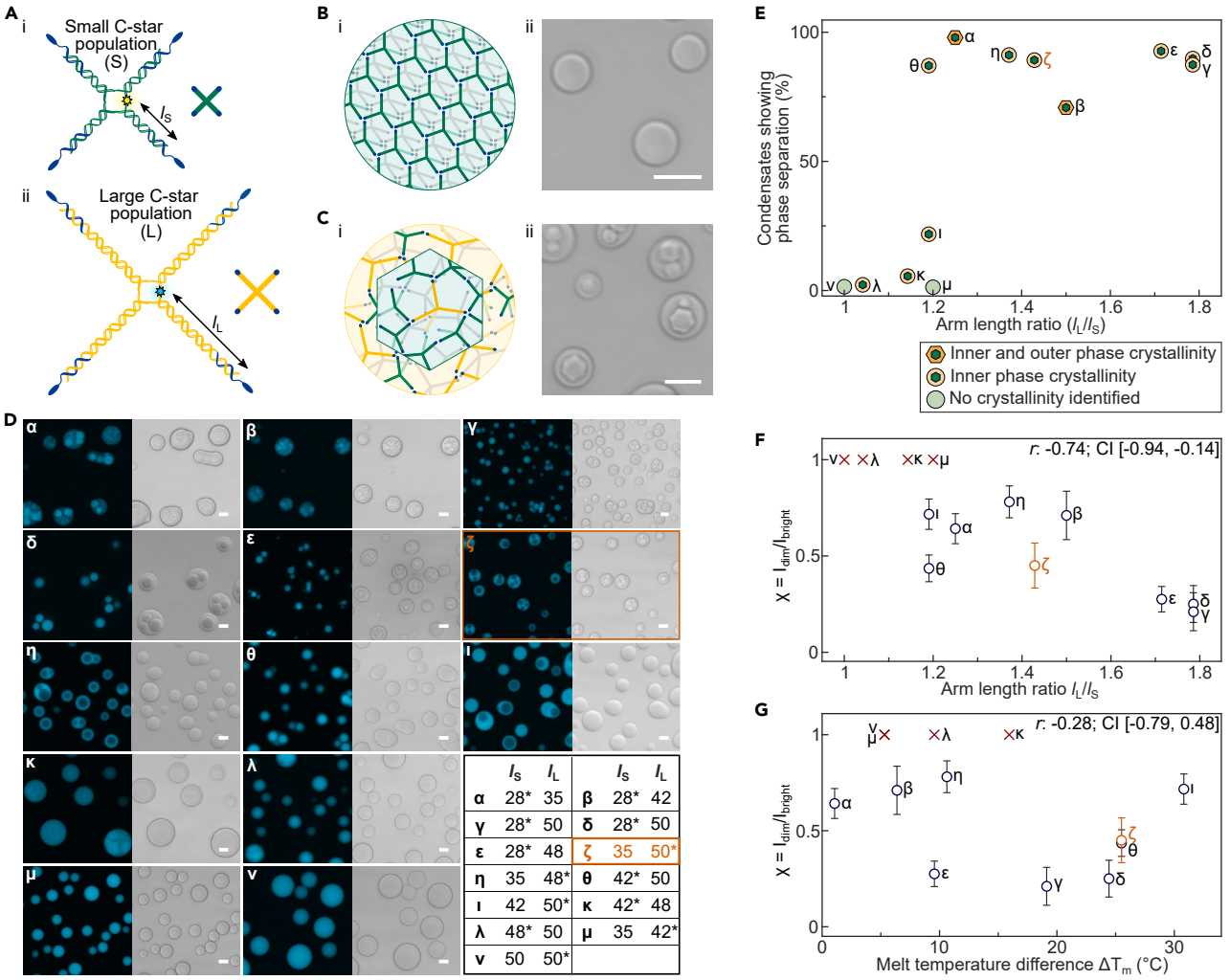

	l_S	l_L		l_S	l_L
α	28*	35	β	28*	42
γ	28*	50	δ	28*	50
ε	28*	48	ζ	35	50*
η	35	48*	θ	42*	50
ι	42	50*	κ	42*	48
λ	48*	50	μ	35	42*
ν	50	50*			

Figure 1. Size-induced phase separation leads to the emergence of core-shell DNA condensates

(A) Schematics of two amphiphilic DNA nanostar (C-star) populations of different sizes: (Ai) small (S, arm length l_S) and (Aii) large (L, arm length l_L), with simplified schematics adjacent. The end of each arm is functionalized with a cholesterol moiety, and the internal junction may be modified with a fluorophore. See Tables S3 and S4 for design and sequence information of all C-stars used.

(B) Schematic (Bi) and bright-field micrograph (Bii) of condensates formed by C-star motif A1, with a 35 base pair (bp) arm length. Condensates form upon thermal annealing of single-stranded components (see supplemental information section methods), and are held together by hydrophobic interactions between cholesterols.[48,52,53,56] Scale bar, 10 μm.

(C) Schematic (Ci) and bright-field micrograph (Cii) of binary condensates composed of small (l_S = 28 bp) and large (l_L = 50 bp) C-stars, showing a core-shell structure with polyhedral inner domain, indicative of crystalline order. Scale bar, 10 μm.

(D) Confocal micrographs of 13 different binary C-star condensates, each composed of two C-star populations with varying arm lengths and melting temperatures, as summarized in the bottom right and Tables S1 and S2. When core-shell morphology is visible, the small motifs preferentially accumulate in the inner domains. An asterisk (*) marks the C-star population labeled with a fluorescent probe in each binary sample. In orange, we mark sample ζ, the binary system used in further studies. All scale bars, 10 μm.

(E) Phase diagram constructed as detailed in the supplemental information from the combination of microscopy and SAXS data, summarizing condensate microstructure, arm length ratio l_L/l_S, and percentage of condensates visually exhibiting phase separation. A sharp transition is noted at an arm length ratio $l_L/l_S \sim 1.2$, above which de-mixing is likely.

(F) Ratio χ of the fluorescence intensity of the dim (I_{dim}) and bright (I_{bright}) domains of the binary condensates shown in (D), plotted against l_L/l_S (see supplemental information section methods). Data are shown as means (circles) ± standard deviations, with full distributions reported in Figure S4. A negative Pearson correlation coefficient, $r = -0.74$ (95% confidence interval [CI] [−0.94, −0.14]), confirms significant anticorrelation between l_L/l_S and χ.

(G) For the same condensates, χ is shown as a function of the absolute difference in melting temperature of the C-star components, ΔT_m. Here, r is not significantly negative ($r = -0.28$, 95% CI [−0.79, 0.48]), indicating a weak correlation. In (F) and (G), χ was only computed for samples where the fraction of de-mixed condensates exceeded 20%, and only these data were used to compute the r values shown here. r values computed using all data, shown in Table S5, lead to identical conclusions. Figure S6 visualizes the ΔT_m vs. l_L/l_S parameter space mapped by the tested samples.

rate, and ionic conditions.[48,52,53,55] The nano-porous structure of the condensates enables internal diffusion of oligonucleotides and proteins.[50]

In this study, we considered binary systems of "small" (S) and "large" (L) four-armed C-stars with different arm lengths (l_S and l_L, with $l_S \leq l_L$). As sketched in Figure 1A, S and L C-stars possess distinct core strands but may share identical cholesterolized strands (see Tables S1, S2, S3, and S4). Upon co-annealing all single-stranded components, the binary C-star mixtures often formed de-mixed condensates with a core-shell morphology, as rendered in Figure 1Ci and demonstrated experimentally in Figure 1Cii. Because the two C-star components interact through identical cholesterol-cholesterol hydrophobic forces, phase separation is likely mediated by packing considerations driven by size mismatch, similar to de-mixing in binary colloidal mixtures or colloid-polymer systems.[57–61] To test this hypothesis, we characterized 13 different binary C-star systems, labeled α-ν, with different combinations of l_S and l_L, as shown in Figure 1D and listed in Tables S1, S2, and S3.

Confocal micrographs shown in Figures 1D, S1, and S2, where either S or L stars were fluorescently labeled, were analyzed to determine the occurrence and extent of de-mixing (see supplemental information section methods). Consistent with the hypothesis that condensate de-mixing is driven by size mismatch, the phase diagram in Figure 1E shows a clear correlation between the fraction of imaged condensates displaying core-shell morphologies and the ratio between arm lengths, l_L/l_S. In particular, for $l_L/l_S \lesssim 1.2$, condensates were mostly mixed, whereas de-mixing was highly likely above this threshold.

Through segmentation of these confocal images (see supplemental information section methods and Figure S3), we extracted the average fluorescent signal in the dimmer phase (I_{dim}) and the brighter phase (I_{bright}) and computed the ratio $\chi = I_{dim}/I_{bright}$ for each condensate, which can be used a proxy for the difference in composition of the core and shell regions (see Figure S4). Specifically, $\chi \sim 1$ indicates that the fluorescently labeled C-star (either S or L, depending on the sample) has similar concentration in both core and shell, whereas $\chi \sim 0$ signifies that one of the phases is effectively depleted of the fluorescent species. The results, collated in Figure 1F and Table S5, demonstrate a strongly negative correlation between χ and l_L/l_S (Pearson correlation coefficient $r = -0.74$ with 95% confidence interval [CI] [−0.94, −0.14]). Core and shell become compositionally more distinct (small χ) for increasing l_L/l_S, further supporting the hypothesis that de-mixing is underpinned by size mismatch.

As summarized in Figure S5 and Table S3, different C-star designs have different melting temperatures (T_m) and would, therefore, assemble from their ssDNA constituents at different stages of the cooling ramp (see supplemental information section methods and Figure S6 for a summary of the parameter space probed by the binary systems under test). It is thus plausible for the observed de-mixing to emerge from sequential assembly, with the inner core forming initially and then being coated by the outer shell. This kinetic mechanism is, however, ruled out as a primary driver of phase separation by the data in Figure 1G and Table S5, where only a weak, non-significant correlation is noted between χ and the absolute T_m difference (ΔT_m) ($r = -0.28$ with 95% CI [−0.79, 0.48]). Taken together, the data in Figures 1E–1G support the hypothesis that the observed core-shell morphologies emerge as a result of equilibrium, size-induced phase separation between the two C-star components.

We further note that, in all tested samples, the smaller C-stars preferentially accumulate in the core. This may be rationalized with interfacial energy considerations, where the larger motifs are likely to favor the external phase due to a lower surface energy for interaction with water resulting from lower density of hydrophobic moieties compared with the internal phase.[62,63] In many instances, the condensates featured multiple distinct core domains within the same shell. These morphologies likely emerge from coalescence events during the assembly process, whereby merging of the outer phases of initially distinct condensates brings together their respective cores.

Small-angle X-ray scattering (SAXS) was used to explore the microstructure of the binary condensates. The data, collated in Figures S7 and S8, were interpreted as detailed in the supplemental information, leading to structural information summarized in Figure 1E and Table S1 (see also supplemental information section methods). In nine of the binary C-star systems (γ, δ, ϵ, ζ, η, θ, ι, κ, and λ) we observed crystalline order in the inner phase coexisting with an amorphous outer phase. Samples α and β showed crystal phases in both the inner and outer domains. Samples μ and ν, which did not show any phase separation in confocal micrographs (Figures 1D and S2), did not produce sharp diffraction peaks, rather showing broad peaks in scattering profiles consistent with an amorphous microstructure as observed in previous work by Brady et al.[52] All crystal phases observed were identified as body-centered cubic (BCC), the same structure observed in single-component systems of tetravalent C-stars.[52] Allocation of the diffraction patterns to either the inner or the outer phase was done by matching the measured lattice parameters and those recorded for single-component C-star samples with $l = l_S$ or $l = l_L$.[52] Because crystallization of at least one component was seen in all samples visually displaying phase separation, we argue that the emergence of crystalline order may contribute to de-mixing by promoting the exclusion of C-stars of one type from a lattice predominantly composed of the other type, as common in molecular and atomic crystals.[64–66] We finally note that the smaller C-star components of binary samples were far more likely to crystallize than the larger ones, consistent with the observation that increasing arm length disfavors crystallization.[52]

Size-induced phase separation is a simple but robust bottom-up approach for establishing addressable microenvironments within cell-like condensates, reminiscent of intracellular phase separation.[67] Distinct from hierarchical and multi-step self-assembly protocols,[42,43,54] the thermodynamic mechanism underpinning our core-shell architectures allows them to form in a simple, one-stage thermal anneal, facilitating sample preparation. In addition, the degree and occurrence of phase separation can be prescribed via straightforward design variations.

Targeted disassembly of C-star domains

We next proceeded to demonstrate the potential of size-induced phase separation as a means of localizing different functionalities in different regions of the condensates. For the remainder of this work, we primarily focused on binary mixtures of smaller C-stars labeled "A" and larger "B" motifs, with arm lengths l_A = 35 base pair (bp) and l_B = 50 bp (Figure 2A). These dimensions correspond to mixture ζ in Figure 1 (highlighted in orange), which robustly formed core-shell condensates. Various designs for A-type (A1 and A2) and B-type (B1, B2, and B3) C-stars were used, hosting different modifications as detailed in Tables S3 and S4. Figure 2B shows a schematic (Figure 2Bi) and micrographs (Figure 2Bii) of core-shell condensates formed by components A1 and B2, whereas Video S1 shows a confocal and bright-field z stack of A1-B3 condensates.

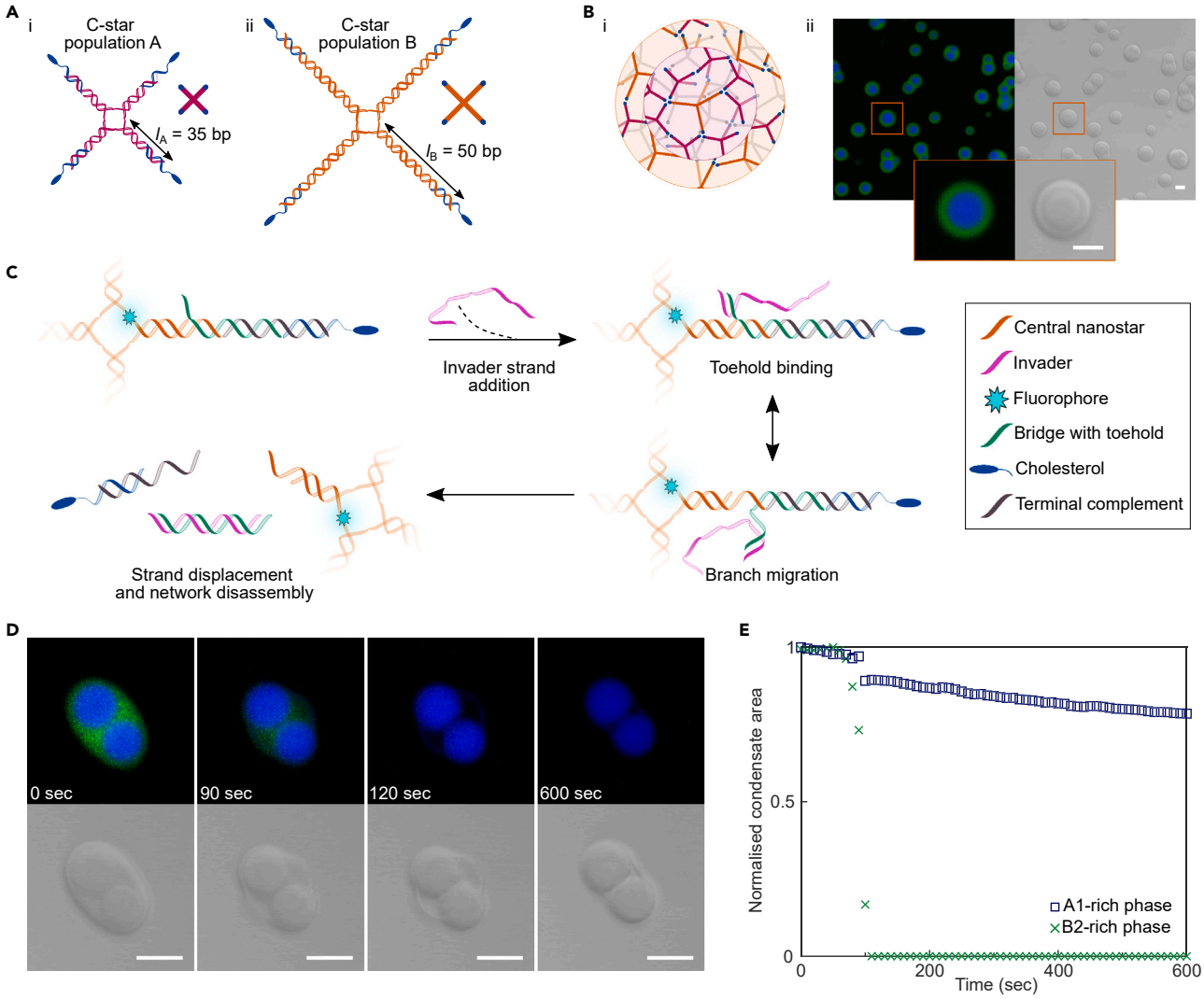

Figure 2. Size-induced phase separation enables phase-targeted disassembly

(A) Schematic of two C-star populations, A with arm length l_A = 35 bp (Ai) and B with arm length l_B = 50 bp (Aii). Multiple A-type and B-type designs with different functionalities were used (A1, A2, B1, B2, and B3; see Tables S3 and S4). Simplified schematics adjacent.

(B) Schematic (Bi) and confocal and bright-field micrographs (Bii) of binary condensates of Cy5-labeled A1 C-stars (blue) and fluorescein-labeled and B2 C-stars (green). Scale bars, 10 μm.

(C) Schematic of C-star disassembly driven by TMSD.[52] An invader strand binds to the toehold and displaces a bridge strand, triggering condensate disassembly by dissociating the central C-star junction from cholesterol-DNA micelles.

(D) Confocal and bright-field micrographs showing the targeted disassembly of the outer phase of the binary condensate described in (B), exploiting TMSD as shown in (C), which acts upon B2-type C-stars primarily present in the shell region. Time stamps mark time elapsed after adding the invader strand. Scale bars, 10 μm.

(E) Disassembly of the condensate shown in (D) quantified by monitoring the cross-sectional area of the two phases measured with image segmentation. Abrupt disassembly is seen for the outer, B2-rich, phase. The A1-rich inner phase shows a small, sharp shrinkage when the outer phase disassembles, ascribed to the presence of B2 motifs in the A1-rich phase (incomplete de-mixing). The steady decrease in apparent area of the A1-rich phase is an artifact of photobleaching. Additional examples are shown in Figures S10–S12 and Video S2.

As a first example of spatially distributed functionality, we sought to enable the triggered disassembly of a selected C-star phase within the condensates, hence inducing a programmable, localized morphological response. Selective network disassembly relied on toehold-mediated strand displacement (TMSD), whereby an invader oligonucleotide displaces a DNA strand initially linking the sticky cholesterol

moiety with the nanostar, as described in earlier work by Brady et al.[52] and shown in Figure 2C. Following disassembly, the targeted C-star motifs split into non-cholesterolized DNA stars and dispersed cholesterol-DNA micelles.[52]

Figure 2D shows phase-separated binary condensates in which B2 motifs (fluorescein labeled, green) are designed to disassemble, whereas A1 C-stars are non-responsive (Cy5-labeled, blue). Condensate disassembly following the addition of the invader strand can be observed as loss of signal from the B2 channel. Figure 2E shows the time evolution of the cross-sectional area of the A-rich and B-rich phases for the condensate in Figure 2D, confirming the abrupt disassembly of the outer shell. Delay in the disassembly following invader addition (t = 0) results from its slow diffusion through the imaging chamber, whereas the progressive decrease in apparent area of the A-rich phase likely arises from the effect of photobleaching (visible in Figure 2D) on the image segmentation pipeline (see supplemental information section methods). We also note a small, but sharp, decrease in the apparent area of the A-rich phase simultaneous with B-phase disassembly. This shrinking response is likely a consequence of the disassembly of B-type motifs initially present in the A-rich phase, and the consequent relaxation of the remaining condensate. Incomplete de-mixing, namely, the presence of B-type motifs in the A-rich phase (and vice versa), is expected in the binary condensates and is reflected in the value of $\chi \sim 0.45$ recorded in Figures 1F and 1G for sample ζ. Bright-field micrographs in Figure 2D confirm the disassembly of most of the outer phase. However, low-density (low-contrast) material is left behind after the green phase has disappeared, which progressively coalesces with the A1-rich cores. Contrast enhancement of the fluorescence images, shown in Figure S9, reveals a weak signal in the Cy5 channel, identifying the low-density material as being composed of A-type C-stars initially present in the B-rich shell, consistent with incomplete de-mixing. The leftover material also prevents the distinct A-rich cores from dispersing after shell disassembly. Further examples of phase-targeted disassembly in A1-B2 condensates are shown in Figures S10–S12 and Video S2. Similar behavior is observed in the disassembly of B3 C-stars in binary A1-B3 condensates, shown in Video S3.

SUVs accumulate at the interface of C-star condensates, forming a lipid shell

Having shown how phase separation in multicomponent C-star condensates enables spatial engineering of functionality, we proceeded to boost their biomimetic relevance by introducing a lipid layer. Small unilamellar lipid vesicles (SUVs), prepared from the zwitterionic lipid 1,2-dioleoyl-sn-glycero-3-phosphocholine (DOPC) and stained with fluorescent Texas Red-labeled 1,2-dihexadecanoyl-sn-glycero-3-phosphoethanolamine (DHPE, at 0.8% molar ratio), were introduced into samples of pre-formed, single-component condensates (supplemental information section methods). SUV diameter was confirmed as ~100 nm by dynamic light scattering, shown in Figure S13. As sketched in Figure 3A, we observed adhesion of SUVs on the surface of the condensates, which appear to assemble into a continuous layer in confocal micrographs (Figure 3A, bottom right). As sketched in Figure 3A (right), SUV adhesion is most likely mediated by the insertion of the C-star cholesterol moieties within the phospholipid bilayer—a known effect exploited for membrane functionalization with DNA nanostructures.[68–73]

In a related system, Walczak et al. reported the adhesion of small C-star aggregates onto the surface of cell-size giant unilamellar vesicles (GUVs),[51,54] observing that small C-star particles are able to permeabilize liposomes and cause their rupture. To assess whether similar destabilization occurs for SUVs depositing onto cell-size C-star condensates, we encapsulated calcein inside SUVs lacking phospholipid

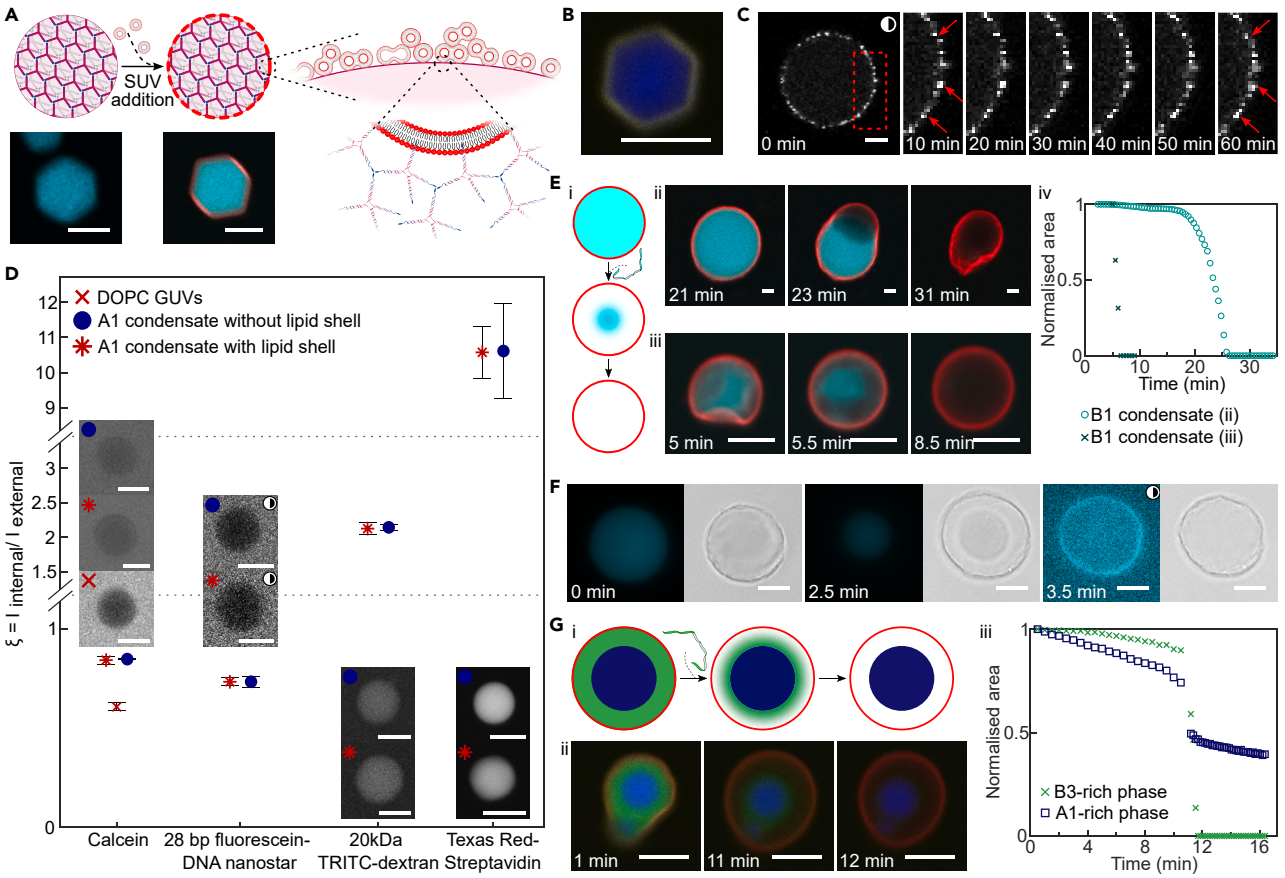

Figure 3. Liposome deposition leads to the formation of a porous lipid shell, which remains stable after condensate etching

(A) Top: schematic of the lipid shell formed from the deposition of DOPC small unilamellar lipid vesicles (SUVs) on C-star condensates. Inset: proposed microstructure. Bottom left: confocal micrograph of a Cy5-labeled A1 condensate (cyan) without a lipid shell. Bottom right: confocal micrograph of a fluorescein-labeled D1 condensate (cyan) with a Texas Red DHPE-labeled lipid shell (red). Scale bars, 10 μm.

(B) Confocal micrograph of a Cy5-labeled A1 C-star condensate (blue) with a lipid shell formed by calcein-loaded SUVs. Calcein fluorescent signal (yellow) demonstrates content retention in the adhered SUVs. Scale bar, 10 μm.

(C) Confocal images showing the adhesion and lack of diffusion of SUVs on the surface of a C1 C-star condensate (arm length 48 bp). One in 800 SUVs are labeled with Texas Red DHPE (white), the remainder are non-fluorescent. Time stamps mark the time elapsed after acquiring the first image. Scale bar, 20 μm.

(D) Partitioning of fluorescent molecular probes into A1 C-star condensates with and without a lipid shell, gauged using the ratio ξ of probe fluorescence intensity inside ($I_{internal}$) and outside the condensate ($I_{external}$), measured from confocal micrographs (examples in insets). Symbols mark the mean of three independent repeats in which a median of 12 condensates were sampled, and error bars show the standard error. Data show that the lipid shell is permeable to the tested probes and that dextran and streptavidin preferentially accumulate within the condensates due the hydrophobic nature of TRITC and Texas Red. For calcein, ξ is also estimated for a sample of DOPC giant unilamellar vesicles (GUVs), nominally impermeable to the dye. Scale bars, 10 μm.

(E) Schematic (Ei) and confocal micrographs (Eii and Eiii) of TMSD triggering disassembly of fluorescein-labeled B1 C-star condensates (cyan) encased in a Texas Red DHPE-labeled lipid shell (red). Time stamps mark time elapsed after invader strand addition. (Eiv) Disassembly of the condensates shown in (Eii) and (Eiii) quantified by monitoring the cross-sectional area of the condensates with image segmentation. Delays in onset of disassembly are a consequence of invader strand diffusion. Additional examples are shown in Figures S15–S17 and Videos S4 and S5. Scale bars, 10 μm.

(F) Epifluorescence and bright-field micrographs of TMSD disassembly of a fluorescein-labeled B1 condensate (cyan) encased in a non-fluorescent lipid shell. Time stamps mark time elapsed after adding the invader strand. After complete disassembly, at 3.5 min, enhancing the contrast of the cyan channel shows a fluorescent ring co-localized with the lipid shell, which remains after disassembly. Scale bars, 10 μm.

(G) Schematic (Gi) and confocal micrographs (Gii) showing TMSD disassembly of B3 C-stars in a binary condensate composed of C-star motifs A1 (Cy5-labeled, blue) and B3 (fluorescein-labeled, green) encased in a lipid shell (Texas Red DHPE-labeled, red). (Giii) Disassembly of the condensate shown in (Gii) quantified by monitoring the cross-sectional area of the two phases measured with image segmentation. As in Figure 2G, we observe abrupt disassembly of the outer, B3-rich, phase, here accompanied by a slight shrinkage of the A1-rich inner phase. Additional examples are shown in Figures S20–S22 and Video S8. Scale bars, 10 μm.

For images marked with a half-shaded circle, contrast enhancement has been applied to aid visualization (see supplemental information section methods).

fluorescent labeling. Figure 3B shows that the calcein signal (shown in yellow) remains localized on the condensate surface, confirming that (at least some of) the SUVs are not disrupted nor rendered leaky. We then prepared lipid shells in which only a small fraction of the SUVs (1 in 800) were doped with Texas Red DHPE, whereas the remainder consisted entirely of unlabeled lipids. As shown in Figure 3C, we observed a speckled pattern on the lipid layer, whose persistence over time demonstrates that neighboring SUVs are unable to exchange fluorescent lipids and are thus not undergoing significant fusion. Monitoring the speckle arrangement over time shows no Brownian motion, indicating that the SUVs remain effectively static over experimentally relevant timescales. Taken together, the absence of substantial leakiness and lack of lipid exchange or diffusion hints at a morphology of the lipid layer as depicted in Figure 3A, in which the SUVs mostly retain their identity rather than reconfiguring into a continuous bilayer.

It is thus expected that the lipid layer would have significant porosity. This hypothesis is tested in Figure 3D, where we used confocal microscopy to measure the permeability of the lipid layer. C-star condensates formed from the A1 motif, either with or without a lipid shell, were soaked in solutions of various fluorescent probes. The ratio (ξ) of fluorescent intensities recorded within ($I_{internal}$) and outside ($I_{external}$) the condensates was used as a proxy to determine whether the lipid shells are permeable to these probes (see supplemental information section methods).[52] For all tested probes, which included calcein, a non-cholesterolized fluorescein-labeled DNA nanostar with 28 bp arm length, 20 kDa tetramethylrhodamine isothiocyanate (TRITC)-labeled dextran, and Texas Red-labeled streptavidin, we observe that ξ is unaffected by the lipid shell. This evidence confirms that the shell possesses pores sufficiently large to allow for diffusion of all tested probes. As a comparison, we present data for penetration of the smallest probe, calcein, into electroformed GUVs, which should be largely impermeable to the dye. As expected, ξ is significantly lower for GUVs compared with condensates, although greater than zero due to out-of-plane fluorescence signals. We also note that dextran and streptavidin accumulate within the condensates, driven by favorable hydrophobic interactions between the cholesterol moieties and the hydrophobic, rhodamine-derived fluorophores they host.[52] A similar test shows that shell porosity is not reduced with longer condensate-SUV incubation times (Figure S14).

Single-component condensates in Figures 3A–3C adopted either a spherical or polyhedral morphology. Variability in aggregate morphology is expected both across and within samples, but, regardless of shape, the underlying microstructure of the material is expected to be crystalline.[50,52]

Lipid shells remain stable after condensate disassembly

The porosity of the lipid shell enables rapid exchange of material, which we can exploit to externally trigger the disassembly response discussed earlier, through the addition of an invader strand. In Figure 3E, we observe condensates of responsive B1 C-stars dissolving from within the lipid shell, confirming that the latter is sufficiently porous to first allow inward diffusion of the invader and, later, the escape of the disassembled DNA fragments (the largest of which is a non-cholesterolized DNA star with 12 bp arm length). Surprisingly, we observe that, in the vast majority of cases, the lipid shells remain stable after condensate disassembly is complete. Therefore, despite the previously noted evidence that SUVs largely retain structural identity (Figures 3B and 3C), a mechanism must exist through which the SUVs remain physically connected, as we will discuss further.

Lipid-coated condensates display diverse responses upon disassembly, two examples of which are shown in Figure 3E. In Figure 3Eii, the condensate disassembles asymmetrically, and a "bubble" is formed, which deforms the lipid shell. In Figure 3Eiii, disassembly occurs more symmetrically, but, as before, an expansion and smoothing of the lipid shell is observed. Although the behaviors differ, both examples suggest an initial buildup in osmotic pressure within the lipid shell due to the release of freely diffusing DNA nanostructures.[20]

In another example, shown in Figure S15 and Video S4, small bubbles initially form, causing local expansion of the lipid shell, followed by an overall contraction and wrinkling that may be caused by the shrinking DNA condensate pulling on the lipid layer, besides the loss of structural support. Shell shrinkage is often observed at later times of the condensate disassembly process and appears to be irreversible (see Figures S16 and S17 and Video S5). DNA nanostructures produced as a result of TMSD disassembly, illustrated in Figure 2C, are found to diffuse out through the pores in the shell, indicating that the lipid shell remains highly porous after condensate disassembly (see Figures 3E and S15–S17 and Videos S4 and S5). Figure 3Eiv shows the time-dependent cross-sectional area of the DNA condensates, confirming abrupt disassembly upon invader addition for the examples in Figures 3Eii and 3Eiii. The different onset times noted for the two condensates are a consequence of the delayed diffusion of the invader in the imaging chamber (supplemental information section methods). Further examples of disassembly traces, including sample averages, are shown in Figures S15–S17. Disassembly of lipid-coated DNA condensates can also be performed by non-specific means, namely, using DNase I. This is demonstrated in Figure S18, where the lipid shell is also observed to persist once disassembly of a C-star condensate (population D1, arm length 28 bp) is completed.

Figure 3F shows the TMSD disassembly of a fluorescently labeled B1 condensate coated in a non-fluorescent lipid shell. As expected, the fluorescent signal from the DNA in the condensate disappears as disassembly progresses. However, on enhancing image contrast post etching, we note a faint signal co-localized with the lipid shell (Figure 3F, right). Video S6 shows a confocal z stack of a Texas Red-labeled lipid shell remaining after disassembly of a fluorescein-labeled B1 condensate—with the contrast of the fluorescent channels enhanced, the same co-localization of the DNA and lipid fluorescent signals is noted. We argue that a small amount of DNA nanostructures may fail to disassemble in the region immediately in contact with the lipid shell, or in the gaps between the SUVs, possibly due to poor accessibility of the toehold domain. This protective effect of the lipids may be reminiscent of the one observed by Julin et al., who found that cationic lipid-coated DNA origami were significantly more resistant to DNase I digestion than non-coated origami.[74]

It is thus reasonable to hypothesize that residual amphiphilic DNA material may play a role in conferring stability to the lipid shell following condensate disassembly by cross-linking neighboring SUVs. DNA-mediated SUV cross-linking would be compatible with the observations reported in Figures 3B and 3C concerning the lack of content leakage and lack of significant lipid exchange between the SUVs in the shell. Nonetheless, other DNA-independent mechanisms may still play an important role, such as membrane adhesion or SUV hemifusion, encouraged by the presence of amphiphiles.[75,76]

The ability to create semi-permeable lipid shells, combined with that of building condensates with distinct regions hosting addressable functionality (see Video

S7), offers a route to construct architectures that resemble a prototypical biological cell. As shown in Figure 3G, this can be achieved by forming a lipid shell around a binary A1-B3 condensate, in which the B3-rich outer phase can be disassembled with TMSD. Upon disassembly, a three-dimensional cavity, reminiscent of a cytoplasm, is formed between the lipid shell and the A1-rich "organelles." In Figure S19, we observe a similar gap formed from the disassembly of the B3 motif in A1-B3 binary condensates enveloped in a lipid shell comprising SUVs encapsulating calcein. Here, we note the calcein signal persisting, indicating a lack of significant content leakage. As demonstrated in Figure 2G, disassembly can be quantified by monitoring the cross-sectional area of the core and shell regions. Consistently, in Figure 3Giii, we note a sharp, complete disassembly transition for the B-rich phase and a simultaneous shrinkage of the A-rich core. Additional examples and averaged data are collated in Figures S20–S22 and see also Video S8.

In situ transcription triggers morphological changes in DNA-based synthetic cells

In a recent contribution, Leathers et al. showed that C-stars can be modified with DNA templates, which are transcribed by T7 RNA polymerase to produce RNA aptamers *in situ*, thus allowing the DNA-based synthetic cells to produce new nucleic acid building blocks.[50] Here, we seek to combine these transcription capabilities with the more complex cell-like architectures we present, which differ from the implementation of Leathers et al. by featuring regions with distinct physical characteristics and composition.

We consider binary systems of C-stars that differ both in size and functionality, sketched in Figure 4A. One population is composed of B1 C-stars (50 bp arm length), which host a modification enabling disassembly through TMSD, as described previously. The second population comprises A2 C-stars (35 bp arm length), which are modified so that an overhang on one of the arms connects to a transcribable ssDNA template (T) through a ssDNA bridge (B) strand—see inset in Figure 4A. The template codes for an extended and brighter version of the Broccoli RNA light-up aptamer,[50] which binds to and induces fluorescence in 3,5-difluoro-4-hydroxybenzylidene imidazolinone (DFHBI),[77] whereas the bridge contributes to forming the double-stranded promoter region required to initiate transcription by T7 RNA polymerase.[50,78]

As expected, one-pot annealing of all ssDNA components produces phase-separated condensates, visible in bright-field images (Figure 4Bii, right). However, when labeling the bridge strand with a fluorescent probe (Alexa Fluor 647), confocal images reveal a non-uniform distribution of the bridge and template (BT) duplex in the inner phase, with a greater concentration found at the outer interface of the A-rich core compared with its center (Figure 4Bii, left). We also note a visible signal from the bridge in the outer shell, indicating a significant presence of fluorescently labeled A2 motifs in the B-rich region. A microscopy-informed schematic of the internal morphology of the condensates is sketched in Figure 4Bi.

Control experiments with A2-only condensates, summarized in Figure S23, reveal that the presence of the bulky BT duplex is, in itself, sufficient to produce size-induced phase separation, leading to the appearance of a template-enriched shell and a template-depleted core, as visible by comparing condensates lacking and including BT strands (Figures S23A and S23B, respectively). An analogous accumulation of extended DNA nanostars at the outer interface of DNA nanostar droplets was recently reported by Tschurikow et al.[79] We thus argue that the non-uniform

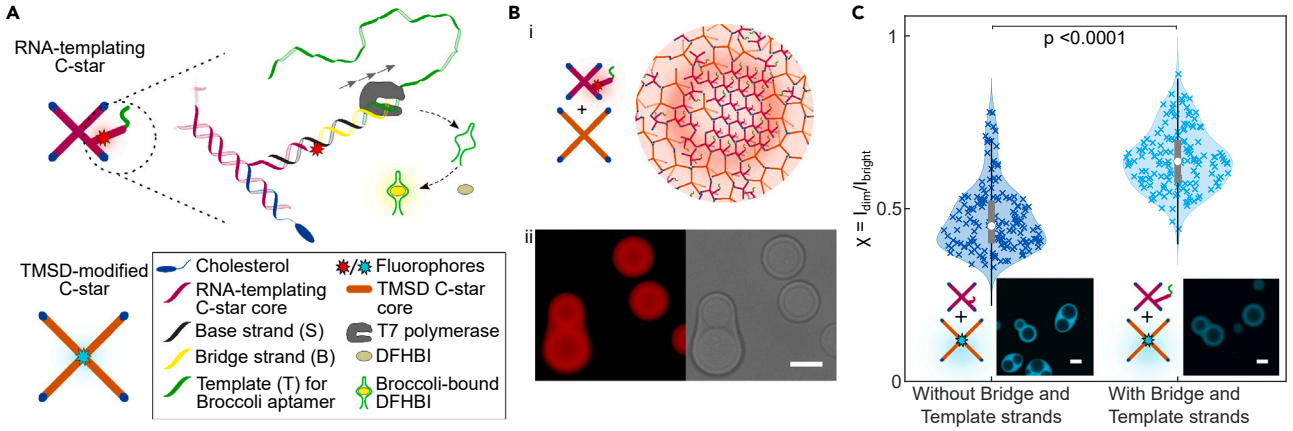

Figure 4. Modification of the DNA building blocks with transcribable constructs influences phase separation

(A) Simplified schematics of two C-star populations, one modified to introduce a DNA template transcribable by T7 RNA polymerase[50] and another modified for TMSD disassembly. Inset shows the ssDNA base (S) and bridge (B) strands linking the transcribable ssDNA template (T) to the core nanostar. The bridge may be labeled with Alexa Fluor 647, and also contains a DNA sequence which, when hybridized with the complementary sequence on the template strand, comprises the double-stranded T7 promoter sequence marking the transcription start site. The template codes for an extended version[50] of the RNA Broccoli aptamer, which binds to and induces fluorescence in DFHBI.[77]

(B) Schematics (Bi) and confocal and bright-field micrographs (Bii) of a binary condensate composed of both the RNA-templating C-star A2 and TMSD-modified C-star B1, where the former has been labeled with a fluorescent probe on the bridge strand, showing the non-uniform distribution of the fluorescent signal from the bridge strand. Scale bar, 10 μm.

(C) Ratio χ of fluorescence intensity of the dim inner phase (I_{dim}) and bright outer phase (I_{bright}) of binary condensates composed of A2 and B1 C-stars, where the B1 motif is labeled with fluorescein and the A2 C-stars either contain all component strands or exclude B and T strands. Data show that the fluorescein-labeled B1 C-stars partition more strongly into the outer phase of the binary condensate when the BT duplex is not present; i.e., phase mixing increases with the introduction of the BT duplex. χ was calculated for 160 condensates annealed without the BT duplex and 145 condensates annealed with the duplex across two independent repeats per condition. Statistical significance was calculated using the two-sample t test, yielding a $p < 0.0001$. Violin plots show the median (white circle) and interquartile range (gray rectangle) of the data, with whiskers reaching $\pm 1.5\times$ interquartile range from the first and third quartiles, shading showing a kernel density estimate of the data, and crosses marking the individual data points. Scale bars, 10 μm.

template distribution seen in Figure 4B for binary condensates could be a direct consequence of size-induced phase separation caused by the template.

Aside from exhibiting a non-uniform distribution, due to its substantial contribution to the molecular weight of the A-type stars, the BT construct may also influence the degree of phase separation between A-type and B-type motifs in the binary condensates. To test this hypothesis, we prepared binary condensates composed of fluorescein-labeled B1 C-stars and unlabeled A2 C-stars, the latter of which either contained or did not contain the BT strands. Confocal microscopy confirms that in both condensate types, the outer phase is enriched in fluorescein-labeled B1 C-stars (shown in cyan in Figure 4C). Image segmentation reveals a significantly higher value of the mixing parameter χ for samples with BT constructs, indicating that the modifications hinder A-B phase separation, likely by making the steric encumbrance of A-type motifs closer to that of B-type motifs.

Having characterized phase separation and BT-distribution in A2-B1 binary mixtures, we proceeded to create cell-like architectures able to sustain transcription, henceforth referred to as synthetic cells. To this end, the BT-containing A2-B1 binary condensates were coated in a lipid shell as discussed above and washed multiple times to remove any free DNA and unattached SUVs (see supplemental information section methods). The removal of freely diffusing Broccoli-templating DNA was verified with transcription reactions run using the supernatants extracted after each wash, as shown in Figure S24A. The B1 motifs were then disassembled with TMSD, as

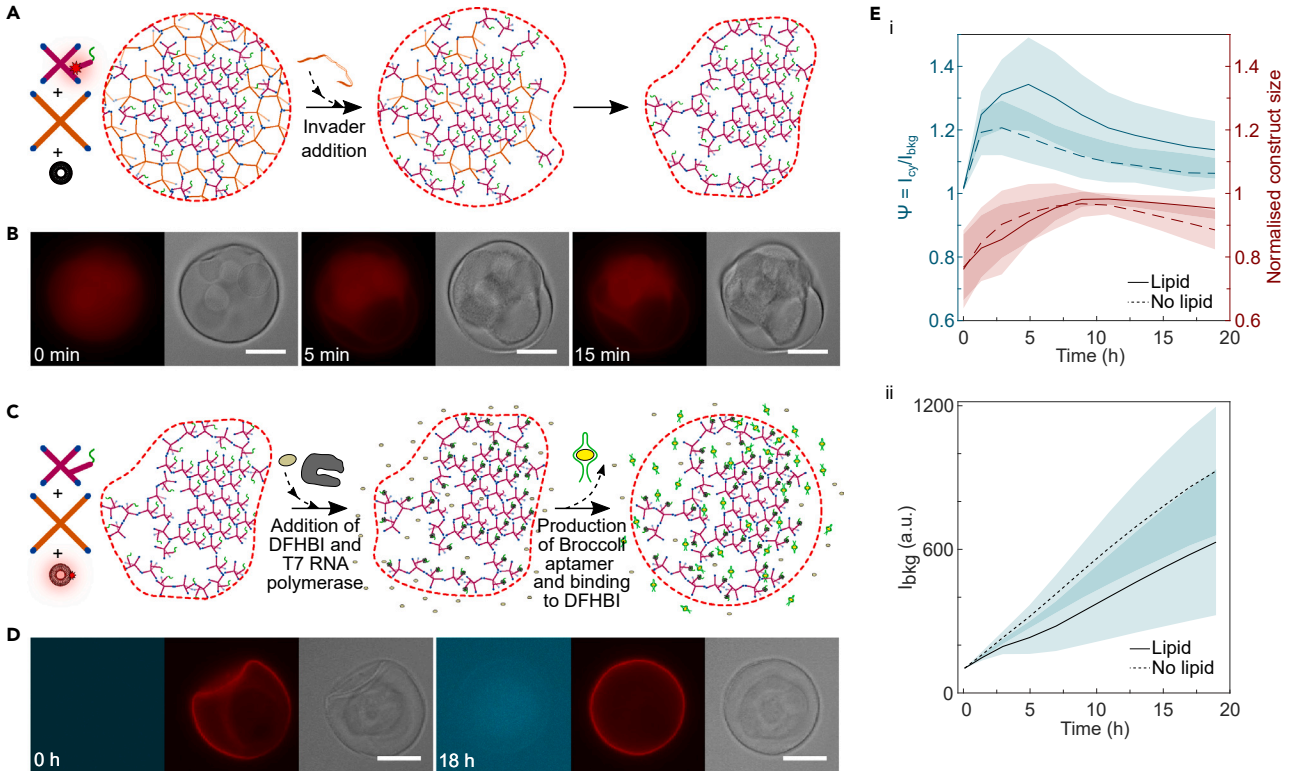

Figure 5. RNA synthesis induces morphological changes in synthetic cells

(A) Schematic showing the disassembly of B1 C-stars in a lipid-coated A2-B1 binary condensate (synthetic cell), triggered by the addition of an invader strand inducing a TMSD reaction (Figure 2D).

(B) Bright-field and epifluorescence micrographs showing the TMSD reaction sketched in (A). In the fluorescent images, the red signal marks the location of the bridge strand labeled with Alexa Fluor 647. Lipids and other DNA components are unlabeled. Note that etching of the B1-rich phase leads to shrinking of the synthetic cell. From the bright-field images, one can observe the re-structuring of the outer C-star phase following TMSD, which forms a mesh-like layer surrounding the A2-rich cores. Time stamps mark time elapsed after invader strand addition. Scale bars, 20 μm.

(C) Schematic showing template transcription and Broccoli synthesis in post-TMSD synthetic cells, where the lipid shell is labeled with a fluorescent probe.

(D) Bright-field and epifluorescence micrographs of the process depicted in (C). The fluorescence signal from Broccoli·DFHBI, shown in cyan (left), increases over time and is accompanied by swelling of the synthetic cell. The Texas Red-labeled lipid shell is shown in red (middle) and is observed to remain intact during transcription. Time stamps mark time elapsed after addition of T7 RNA polymerase and transcription mixture (see supplemental information section methods). Scale bars, 20 μm.

(E) Quantification of Broccoli synthesis and morphological changes for synthetic cells undergoing transcription, where the lipid shell is non-fluorescent and the bridge strand is labeled with Alexa Fluor 647 (as in A, B, Figures S26, and S27 and Videos S12, S13, S14, S15, S16, and S17). (Ei) Left axis: ratio ψ between the fluorescence intensity of Broccoli·DFHBI sampled from epifluorescence micrographs in the region surrounding the A2-rich core ("cytoplasm") of the synthetic cells, and in the surrounding solution (I_{bkg}). Right axis: condensate size. (Eii) Time dependence of I_{bkg}. Solid lines and dashed lines are relative to synthetic cells featuring or lacking a lipid shell, respectively. For both (Ei) and (Eii), data are extracted through image segmentation (see supplemental information section methods and Figure S11) of 23 lipid-coated (solid line) condensates and 16 non-coated (dashed line) synthetic cells; with lines showing the mean and shaded regions indicating the mean ± the standard deviation of the data.

sketched in Figure 5A. Epifluorescence images show a significant quantity of labeled RNA-templating A2 C-stars (red) in the B1-rich outer phase pre-etching, as expected given the hindering effect that the BT duplex has on A-B de-mixing, quantified in Figure 4C. During disassembly of the B1 C-stars, some of the BT-linked A2 motifs collapse to form a low-density mesh surrounding the core of the synthetic cells. Other constructs were able to detach and escape the lipid shells, as confirmed by control experiments in which RNA transcription reactions are carried out with the supernatants removed from the samples post-B1 etching and summarized in Figure S24B. Despite the synthetic cells having been sufficiently washed pre-etching

(Figure S24A), the Broccoli signal from the supernatant was again substantial post-etch, indicating a significant leakage of the Broccoli-templating A2 constructs during removal of the outer phase (Figure S24B). Bright-field micrographs in Figure 5B also show the lipid shell shrinking and wrinkling as a result of a possible pulling action from the collapsing shell material and the loss of structural support, as noted when discussing Figures 3E and S15.

Transcription of the etched and subsequently washed synthetic cells causes an expected increase in Broccoli fluorescent signal, and a distinct morphological response, both of which are sketched in Figure 5C and shown in epifluorescence micrographs in Figure 5D. Broccoli fluorescence builds up within the A2-rich dense inner phase, within the cytoplasm-like region and low-density material left behind by B1 disassembly, and later in the medium surrounding the synthetic cells. More surprisingly, we note a dramatic change in the morphology of the disordered A2-rich mesh surrounding the core of the synthetic cells, which expands and inflates the synthetic cell to a size and shape akin to that observed prior to etching. Additional images and further examples of the transcription-induced synthetic-cell expansion can be found in Figures S25–S27 and Videos S9, S10, S11, S12, S13, S14, S15, S16, and S17. Fluorescent labeling of the SUVs used in Figures 5D and S25 and Videos S9, S10, and S11 demonstrates that the lipid shell follows the expansion the synthetic-cell pseudo-cytoplasm, which, however, also swells in the absence of lipids, as shown in Figure S26 and Videos S15, S16, and S17.

In order to rationalize this morphological response, we used image analysis to extract the outer dimensions of the synthetic cells and the intensity of the Broccoli fluorescence signal, measured both in the solution surrounding the synthetic cells (I_{bkg}) and in their cytoplasm (I_{cy}, see Figure S28). The results of this analysis are presented in Figure 5Ei for synthetic cells prepared with the Alexa Fluor 647-labeled bridge strand, with or without a (non-fluorescent) lipid shell. Regardless of the presence of a lipid shell, construct size increases as transcription progresses and reaches a maximum after approximately 8 h, followed by a slight decrease in size, which is less pronounced for the lipid-coated synthetic cells. The fluorescence intensity ratio $\psi = I_{cy}/I_{bkg}$ should approximate the ratio of aptamer concentrations inside and outside the constructs. As might be expected, at early times, we see a pronounced growth of ψ from its initial value of $\sim$1 due to localized Broccoli transcription within the synthetic cells. A maximum is then reached, followed by a steady decrease back toward $\psi \sim 1$, due to aptamer leakage and the consequent increase of I_{bkg} (also notable in Figures S26 and S27 and Videos S12, S13, S14, S15, S16, and S17), combined with the progressive reduction in polymerase activity. A clear difference is observed between lipid-coated and non-coated constructs, with the former displaying a higher maximum ψ value, which is also reached at later times. These differences indicate that, albeit permeable, the lipid shell is able to slow down outward diffusion of the Broccoli aptamer. This hypothesis is consistent with the absolute values measured for I_{bkg}, which are higher for lipid-less constructs compared with the complete synthetic cells, as shown in Figure 5Eii. The accumulation of the Broccoli aptamer within the synthetic cells (whether lipid-coated or not) hints at a potential mechanism for the observed size increase, where a transient osmotic pressure buildup from the transcript causes swelling of the low-density A2-rich material remaining around the cores of the constructs following removal of the B1-rich shell. A similar response was observed by Saleh et al. during the enzymatic digestion of DNA hydrogel droplets, where the formation of internal cavities was ascribed to osmotic pressure from disassembled DNA fragments.[20]

DISCUSSION

We have presented a strategy for constructing cell-like architectures that mimic multiple characteristics of biological cells, including a porous lipid-based shell, a cytoplasm-like cavity, and dense membrane-less internal compartments. These biomimetic devices are produced via bulk self-assembly of amphiphilic DNA nanostructures that undergo size-induced phase separation, combined with liposome deposition and phase-specific etching, hence negating the need for complex microfluidics or emulsion-based methods. The membrane-less organelles can be modified to host a DNA template. This template can be transcribed to produce RNA, whose localized synthesis causes a swelling response in the cytoplasm and lipid shell of the synthetic cells, due to transient osmotic pressure buildup. The ability to initially accumulate and then progressively release nucleic acids of tailored sequence could make our solution a valuable starting point for the development of therapeutic agents, e.g., for vaccines[80] and gene therapy.[81]

Our proof-of-concept implementation dovetails the structural and dynamic control afforded by DNA nanotechnology with amphiphile self-assembly, phase-separation phenomenology, and *in vitro* transcription, hence exemplifying how increasingly complex architectures and responses can be engineered from the bottom-up if complementary molecular tools are synergistically combined. The synthetic-cell assembly strategy we outline is general and can be systematically expanded by localizing functional moieties other than the DNA templates in the coexisting phases, e.g., grafted enzymes[82] or nanoparticles.[83] Despite being used here only to form a semi-permeable shell, the liposomes could further be targeted with lipid-specific functional modification, such as membrane receptors, while their ability to retain contents could be exploited to encapsulate and conditionally release molecular cargoes. Different lipid compositions could also be introduced, for instance to tune the properties of the shell through controlled liposome fusion and its interactions with the condensates via electrostatics, as reported by Aumiller et al. and Pir Cakmak et al., using anionic lipids and polyelectrolyte coacervates.[84,85] This modularity and design versatility further strengthens the applicative outlook of our solution, potentially unlocking the design of multi-functional therapeutic synthetic cells that combine nucleic acid synthesis with targeting abilities and the possibility of co-delivering small-molecule drugs and macromolecules encapsulated in the liposomes and/or embedded in the DNA matrix.[52]

EXPERIMENTAL PROCEDURES

Resource availability

Lead contact

Further information and requests for resources should be directed to and will be fulfilled by the lead contact, Lorenzo Di Michele (ld389@cam.ac.uk).

Materials availability

This study did not generate new materials—novel oligonucleotide sequences are detailed in the supplemental information.

Data and code availability

The datasets generated from this study are available at https://doi.org/10.17863/CAM.101613.

SUPPLEMENTAL INFORMATION

Supplemental information can be found online at https://doi.org/10.1016/j.chempr.2023.10.004.

ACKNOWLEDGMENTS

L.M., L.D.M., and D.A.T. acknowledge support from the European Research Council (ERC) under the Horizon 2020 Research and Innovation Programme (ERC-STG no. 851667—NANOCELL). G.F. acknowledges funding from the Department of Chemistry at Imperial College London. M.P.-P. acknowledges support from a UK Research and Innovation New Horizons Grant (EP/V048058/1) and an EPSRC Doctoral Prize Fellowship (EP/W524323). A.L. and L.D.M. acknowledge support from a Royal Society Research Grant for Research Fellows (RGF/R1/180043). L.D.M. also acknowledges support from a Royal Society University Research Fellowship (UF160152, URF/R/221009). M.J.B. is supported by a Royal Society University Research Fellowship (URF/R1/180172) and acknowledges funding from a Royal Society Enhancement Award (RGF/EA/181009) and an EPSRC New Investigator Award (EP/V030434/2). The authors acknowledge the Facility for Imaging by Light Microscopy (FILM) at Imperial College London and thank Stephen Rothery for his assistance at the facility. The authors acknowledge Diamond Light Source for providing synchrotron beamtime (SM29072) and thank Andy Smith for assistance in operating beamline I22. The authors thank Elisa Franco for useful feedback on the manuscript.

AUTHOR CONTRIBUTIONS

L.M. conducted experiments and data analysis, supported by D.A.T., G.F., R.A.B., M.P.-P., and A.L. L.M. and L.D.M. designed the research, assisted by M.J.B. L.M. and L.D.M. wrote the manuscript. All authors contributed to result interpretation and commented on the manuscript. L.D.M. supervised the research.

DECLARATION OF INTERESTS

The authors declare no competing interests.

Received: May 12, 2023
Revised: August 25, 2023
Accepted: October 9, 2023
Published: November 1, 2023

REFERENCES

1. Schwille, P. (2015). Jump-starting life? Fundamental aspects of synthetic biology. J. Cell Biol. *210*, 687–690. https://doi.org/10.1083/jcb.201506125.

2. Buddingh, B.C., and Van Hest, J.C.M. (2017). Artificial cells: synthetic compartments with life-like functionality and adaptivity. Acc. Chem. Res. *50*, 769–777. https://doi.org/10.1021/acs.accounts.6b00512.

3. Yewdall, N.A., Mason, A.F., and Van Hest, J.C.M. (2018). The hallmarks of living systems: towards creating artificial cells. Interface Focus *8*, 20180023. https://doi.org/10.1098/rsfs.2018.0023.

4. Cameron, D.E., Bashor, C.J., and Collins, J.J. (2014). A brief history of synthetic biology. Nat. Rev. Microbiol. *12*, 381–390. https://doi.org/10.1038/nrmicro3239.

5. Majumder, S., and Liu, A.P. (2017). Bottom-up synthetic biology: modular design for making artificial platelets. Phys. Biol. *15*, 013001. https://doi.org/10.1088/1478-3975/aa9768.

6. Yu, X., Zhou, L., Wang, G., Wang, L., and Dou, H. (2022). Hierarchical structures in macromolecule-assembled synthetic cells. Macromol. Rapid Commun. *43*, e2100926. https://doi.org/10.1002/MARC.202100926.

7. Jia, H., and Schwille, P. (2019). Bottom-up synthetic biology: reconstitution in space and time. Curr. Opin. Biotechnol. *60*, 179–187. https://doi.org/10.1016/J.COPBIO.2019.05.008.

8. Dora Tang, T.Y., Rohaida Che Hak, C., Thompson, A.J., Kuimova, M.K., Williams, D.S., Perriman, A.W., and Mann, S. (2014). Fatty acid membrane assembly on coacervate microdroplets as a step towards a hybrid protocell model. Nat. Chem. *6*, 527–533. https://doi.org/10.1038/nchem.1921.

9. Deshpande, S., Brandenburg, F., Lau, A., Last, M.G.F., Spoelstra, W.K., Reese, L., Wunnava, S., Dogterom, M., and Dekker, C. (2019). Spatiotemporal control of coacervate formation within liposomes. Nat. Commun. *10*, 1800. https://doi.org/10.1038/s41467-019-09855-x.

10. Rubio-Sánchez, R., O'Flaherty, D.K., Wang, A., Coscia, F., Petris, G., Di Michele, L., Cicuta, P., and Bonfio, C. (2021). Thermally driven membrane phase transitions enable content reshuffling in primitive cells. J. Am. Chem. Soc. *143*, 16589–16598. https://doi.org/10.1021/jacs.1c06595.

11. Jahnke, K., Huth, V., Mersdorf, U., Liu, N., and Göpfrich, K. (2022). Bottom-up assembly of synthetic cells with a DNA cytoskeleton. ACS Nano *16*, 7233–7241. https://doi.org/10.1021/acsnano.1c10703.

12. Tran, M.P., Chatterjee, R., Dreher, Y., Fichtler, J., Jahnke, K., Hilbert, L., Zaburdaev, V., Göpfrich, K., Tran, M.P., Dreher, Y., et al. (2022). A DNA segregation module for synthetic cells. Small *19*, 2202711. https://doi.org/10.1002/SMLL.202202711.

13. Mason, A.F., Buddingh', B.C., Williams, D.S., and Van Hest, J.C.M. (2017). Hierarchical self-assembly of a copolymer-stabilized coacervate protocell. J. Am. Chem. Soc. *139*, 17309–17312. https://doi.org/10.1021/jacs.7b10846.

14. Gumz, H., Boye, S., Iyisan, B., Krönert, V., Formanek, P., Voit, B., Lederer, A., and Appelhans, D. (2019). Toward functional synthetic cells: in-depth study of nanoparticle and enzyme diffusion through a cross-linked polymersome membrane. Adv. Sci. (Weinh) *6*, 1801299. https://doi.org/10.1002/ADVS.201801299.

15. Huang, X., Patil, A.J., Li, M., and Mann, S. (2014). Design and construction of higher-order structure and function in proteinosome-based protocells. J. Am. Chem. Soc. *136*, 9225–9234. https://doi.org/10.1021/ja504213m.

16. Booth, R., Qiao, Y., Li, M., and Mann, S. (2019). Spatial positioning and chemical coupling in coacervate-in-proteinosome protocells. Angew. Chem. Int. Ed. Engl. *58*, 9120–9124. https://doi.org/10.1002/ANIE.201903756.

17. Tan, H., Guo, S., Dinh, N.D., Luo, R., Jin, L., and Chen, C.H. (2017). Heterogeneous multi-compartmental hydrogel particles as synthetic cells for incompatible tandem reactions. Nat. Commun. *8*, 663. https://doi.org/10.1038/s41467-017-00757-4.

18. Jeon, B.J., Nguyen, D.T., and Saleh, O.A. (2020). Sequence-controlled adhesion and microemulsification in a two-phase system of DNA liquid droplets. J. Phys. Chem. B *124*, 8888–8895. https://doi.org/10.1021/acs.jpcb.0c06911.

19. Sato, Y., Sakamoto, T., and Takinoue, M. (2020). Sequence-based engineering of dynamic functions of micrometer-sized DNA droplets. Sci. Adv. *6*, eaba3471. https://doi.org/10.1126/sciadv.aba3471.

20. Saleh, O.A., Jeon, B.J., and Liedl, T. (2020). Enzymatic degradation of liquid droplets of DNA is modulated near the phase boundary. Proc. Natl. Acad. Sci. USA *117*, 16160–16166. https://doi.org/10.1073/pnas.2001654117.

21. Hastings, R.L., and Boeynaems, S. (2021). Designer condensates: A toolkit for the biomolecular architect. J. Mol. Biol. *433*, 166837. https://doi.org/10.1016/J.JMB.2021.166837.

22. Li, J., Xu, Z., Zhu, M., Zhao, C., Wang, X., Chen, H., Liu, X., Wang, L., and Huang, X. (2022). Programmable spatial organization of liquid-phase condensations. Chem *8*, 784–800. https://doi.org/10.1016/j.chempr.2021.11.011.

23. Martino, C., and deMello, A.J. (2016). Droplet-based microfluidics for artificial cell generation: A brief review. Interface Focus *6*, 20160011. https://doi.org/10.1098/rsfs.2016.0011.

24. Ai, Y., Xie, R., Xiong, J., and Liang, Q. (2020). Microfluidics for biosynthesizing: from droplets and vesicles to artificial cells. Small *16*, e1903940. https://doi.org/10.1002/smll.201903940.

25. Shum, H.C., Zhao, Y.J., Kim, S.H., and Weitz, D.A. (2011). Multicompartment polymersomes from double emulsions. Angew. Chem. Int. Ed. Engl. *50*, 1648–1651. https://doi.org/10.1002/ANIE.201006023.

26. Deshpande, S., Caspi, Y., Meijering, A.E.C., and Dekker, C. (2016). Octanol-assisted liposome assembly on chip. Nat. Commun. *7*, 10447. https://doi.org/10.1038/ncomms10447.

27. Kamiya, K., and Takeuchi, S. (2017). Giant liposome formation toward the synthesis of well-defined artificial cells. J. Mater. Chem. B *5*, 5911–5923. https://doi.org/10.1039/c7tb01322a.

28. Aufinger, L., and Simmel, F.C. (2018). Artificial gel-based organelles for spatial organization of cell-free gene expression reactions. Angew. Chem. Int. Ed. Engl. *57*, 17245–17248. https://doi.org/10.1002/anie.201809374.

29. Krafft, D., López Castellanos, S., Lira, R.B., Dimova, R., Ivanov, I., and Sundmacher, K. (2019). Compartments for synthetic cells: osmotically assisted separation of oil from double emulsions in a microfluidic chip. Chembiochem *20*, 2604–2608. https://doi.org/10.1002/CBIC.201900152.

30. Tivony, R., Fletcher, M., Al Nahas, K., and Keyser, U.F. (2021). A microfluidic platform for sequential assembly and separation of synthetic cell models. ACS Synth. Biol. *10*, 3105–3116. https://doi.org/10.1021/ACSSYNBIO.1C00371.

31. Zhan, P., Jahnke, K., Liu, N., and Göpfrich, K. (2022). Functional DNA-based cytoskeletons for synthetic cells. Nat. Chem. *14*, 958–963. https://doi.org/10.1038/s41557-022-00945-w.

32. Staufer, O., Estebano Hernandez Bücher, J., Fichtler, J., Schröter, M., Platzman, I., Spatz, J.P., Staufer, O., Hernandez Bücher, J.E., Schröter, M., Platzman, I., et al. (2022). Vesicle induced receptor sequestration: mechanisms behind extracellular vesicle-based protein signaling. Adv. Sci. *9*, 2200201. https://doi.org/10.1002/ADVS.202200201.

33. Lussier, F., Schröter, M., Diercks, N.J., Jahnke, K., Weber, C., Frey, C., Platzman, I., and Spatz, J.P. (2022). pH-triggered assembly of endomembrane multicompartments in synthetic cells. ACS Synth. Biol. *11*, 366–382. https://doi.org/10.1021/acssynbio.1c00472.

34. Hernandez Bücher, J.E., Staufer, O., Ostertag, L., Mersdorf, U., Platzman, I., and Spatz, J.P. (2022). Bottom-up assembly of target-specific cytotoxic synthetic cells. Biomaterials *285*, 121522. https://doi.org/10.1016/J.BIOMATERIALS.2022.121522.

35. Stephanopoulos, G. (2012). Synthetic biology and metabolic engineering. ACS Synth. Biol. *1*, 514–525. https://doi.org/10.1021/sb300094q.

36. SantaLucia, J., Allawi, H.T., and Seneviratne, P.A. (1996). Improved nearest-neighbor parameters for predicting DNA duplex stability. Biochemistry *35*, 3555–3562. https://doi.org/10.1021/bi951907q.

37. Simmel, F.C., Yurke, B., and Singh, H.R. (2019). Principles and applications of nucleic acid strand displacement reactions. Chem. Rev. *119*, 6326–6369. https://doi.org/10.1021/acs.chemrev.8b00580.

38. Zadeh, J.N., Steenberg, C.D., Bois, J.S., Wolfe, B.R., Pierce, M.B., Khan, A.R., Dirks, R.M., and Pierce, N.A. (2011). NUPACK: analysis and design of nucleic acid systems. J. Comput. Chem. *32*, 170–173. https://doi.org/10.1002/jcc.21596.

39. Koh, H., Lee, J.G., Lee, J.Y., Kim, R., Tabata, O., Jin-Woo, K., and Kim, D.N. (2021). Design approaches and computational tools for DNA nanostructures. IEEE Open J. Nanotechnol. *2*, 86–100. https://doi.org/10.1109/OJNANO.2021.3119913.

40. Seeman, N.C. (1982). Nucleic acid junctions and lattices. J. Theor. Biol. *99*, 237–247. https://doi.org/10.1016/0022-5193(82)90002-9.

41. Seeman, N.C., and Sleiman, H.F. (2017). DNA nanotechnology. Nat. Rev. Mater. *3*, 1–23. https://doi.org/10.1038/natrevmats.2017.68.

42. Merindol, R., Loescher, S., Samanta, A., and Walther, A. (2018). Pathway-controlled formation of mesostructured all-DNA colloids and superstructures. Nat. Nanotechnol. *13*, 730–738. https://doi.org/10.1038/s41565-018-0168-1.

43. Samanta, A., Hörner, M., Liu, W., Weber, W., and Walther, A. (2022). Signal-processing and adaptive prototissue formation in metabolic DNA protocells. Nat. Commun. *13*, 3968. https://doi.org/10.1038/s41467-022-31632-6.

44. Sato, Y., and Takinoue, M. (2022). Capsule-like DNA hydrogels with patterns formed by lateral phase separation of DNA nanostructures. JACS Au *2*, 159–168. https://doi.org/10.1021/jacsau.1c00450.

45. Gong, J., Tsumura, N., Sato, Y., and Takinoue, M. (2022). Computational DNA droplets recognizing miRNA sequence inputs based on liquid–liquid phase separation. Adv. Funct. Mater. *32*, 2202322. https://doi.org/10.1002/adfm.202202322.

46. Agarwal, S., Osmanovic, D., Klocke, M.A., and Franco, E. (2022). The growth rate of DNA condensate droplets increases with the size of participating subunits. ACS Nano *16*, 11842–11851. https://doi.org/10.1021/acsnano.2c00084.

47. Agarwal, S., Dizani, M., Osmanovic, D., and Franco, E. (2023). Light-controlled growth of DNA organelles in synthetic cells. Interface Focus *13*, 20230017. https://doi.org/10.1098/RSFS.2023.0017.

48. Brady, R.A., Brooks, N.J., Cicuta, P., and Di Michele, L. (2017). Crystallization of amphiphilic DNA C-stars. Nano Lett. *17*, 3276–3281. https://doi.org/10.1021/acs.nanolett.7b00980.

49. Rubio-Sánchez, R., Fabrini, G., Cicuta, P., and Di Michele, L. (2021). Amphiphilic DNA nanostructures for bottom-up synthetic biology. Chem. Commun. (Camb) *57*, 12725–12740. https://doi.org/10.1039/D1CC04311K.

50. Leathers, A., Walczak, M., Brady, R.A., Al Samad, A., Kotar, J., Booth, M.J., Cicuta, P., and Di Michele, L. (2022). Reaction-diffusion patterning of DNA-based artificial cells. J. Am. Chem. Soc. *144*, 17468–17476. https://doi.org/10.1021/jacs.2c06140.

51. Walczak, M., Mancini, L., Xu, J., Raguseo, F., Kotar, J., Cicuta, P., and Di Michele, L. (2023). A synthetic signaling network imitating the action of immune cells in response to bacterial metabolism. Adv. Mater. *35*, e2301562. https://doi.org/10.1002/ADMA.202301562.

52. Brady, R.A., Brooks, N.J., Foderà, V., Cicuta, P., and Di Michele, L. (2018). Amphiphilic-DNA platform for the design of crystalline frameworks with programmable structure and functionality. J. Am. Chem. Soc. *140*, 15384–15392. https://doi.org/10.1021/jacs.8b09143.

53. Brady, R.A., Kaufhold, W.T., Brooks, N.J., Foderà, V., and Di Michele, L. (2019). Flexibility defines structure in crystals of amphiphilic DNA nanostars. J. Phys. Condens. Matter *31*, 074003. https://doi.org/10.1088/1361-648X/aaf4a1.

54. Walczak, M., Brady, R.A., Mancini, L., Contini, C., Rubio-Sánchez, R., Kaufhold, W.T., Cicuta, P., and Di Michele, L. (2021). Responsive core-shell DNA particles trigger lipid-membrane disruption and bacteria entrapment. Nat. Commun. *12*, 4743. https://doi.org/10.1038/s41467-021-24989-7.

55. Fabrini, G., Minard, A., Brady, R.A., Di Antonio, M., and Di Michele, L. (2022). Cation-responsive and photocleavable hydrogels from noncanonical amphiphilic DNA nanostructures. Nano Lett. *22*, 602–611. https://doi.org/10.1021/acs.nanolett.1c03314.

56. Walczak, M., Brady, R.A., Leathers, A., Kotar, J., and Di Michele, L. (2023). Influence of hydrophobic moieties on the crystallization of amphiphilic DNA nanostructures. J. Chem. Phys. *158*, 84501. https://doi.org/10.1063/5.0132484/2868925.

57. Asakura, S., and Oosawa, F. (1958). Interaction between particles suspended in solutions of macromolecules. J. Polym. Sci. *33*, 183–192. https://doi.org/10.1002/POL.1958.1203312618.

58. Meijer, E.J., and Frenkel, D. (1991). Computer simulation of polymer-induced clustering of colloids. Phys. Rev. Lett. *67*, 1110–1113. https://doi.org/10.1103/PhysRevLett.67.1110.

59. Biben, T., and Hansen, J.P. (1991). Phase separation of asymmetric binary hard-sphere fluids. Phys. Rev. Lett. *66*, 2215–2218. https://doi.org/10.1103/PhysRevLett.66.2215.

60. Imhof, A., and Dhont, J.K.G. (1995). Experimental phase diagram of a binary colloidal hard-sphere mixture with a large size ratio. Phys. Rev. Lett. *75*, 1662–1665. https://doi.org/10.1103/PhysRevLett.75.1662.

61. Harden, J.L., Guo, H., Bertrand, M., Shendruk, T.N., Ramakrishnan, S., and Leheny, R.L. (2018). Enhanced gel formation in binary mixtures of nanocolloids with short-range attraction. J. Chem. Phys. *148*, 044902. https://doi.org/10.1063/1.5007038.

62. Harkins, W.D., Davies, E.C.H., and Clark, G.L. (1917). The orientation of molecules in the surfaces of liquids, the energy relations at surfaces, solubility, adsorption, emulsification, molecular association, and the effect of acids and bases on interfacial tension. 1 (SURFACE ENERGY VI.). J. Am. Chem. Soc. *39*, 541–596. https://doi.org/10.1021/ja02249a002.

63. Waele, A.D. (1926). The manifestation of interfacial forces in dispersed systems. J. Am. Chem. Soc. *48*, 2760–2776. https://doi.org/10.1021/JA01690A002.

64. Meldrum, F.C., and Cölfen, H. (2008). Controlling mineral morphologies and structures in biological and synthetic systems. Chem. Rev. *108*, 4332–4432. https://doi.org/10.1021/cr8002856.

65. Erdemir, D., Lee, A.Y., and Myerson, A.S. (2009). Nucleation of crystals from solution: classical and two-step models. Acc. Chem. Res. *42*, 621–629. https://doi.org/10.1021/ar800217x.

66. Chen, J., Sarma, B., Evans, J.M.B., and Myerson, A.S. (2011). Pharmaceutical crystallization. Cryst. Growth Des. *11*, 887–895. https://doi.org/10.1021/cg101556s.

67. Brangwynne, C.P., Tompa, P., and Pappu, R.V. (2015). Polymer physics of intracellular phase transitions. Nat. Phys. *11*, 899–904. https://doi.org/10.1038/nphys3532.

68. Morzy, D., Rubio-Sánchez, R., Joshi, H., Aksimentiev, A., Di Michele, L., and Keyser, U.F. (2021). Cations regulate membrane attachment and functionality of DNA nanostructures. J. Am. Chem. Soc. *143*, 7358–7367. https://doi.org/10.1021/jacs.1c00166.

69. Chidchob, P., Offenbartl-Stiegert, D., McCarthy, D., Luo, X., Li, J., Howorka, S., and Sleiman, H.F. (2019). Spatial presentation of cholesterol units on a DNA cube as a determinant of membrane protein-mimicking functions. J. Am. Chem. Soc. *141*, 1100–1108. https://doi.org/10.1021/jacs.8b11898.

70. Birkholz, O., Burns, J.R., Richter, C.P., Psathaki, O.E., Howorka, S., and Piehler, J. (2018). Multi-functional DNA nanostructures that puncture and remodel lipid membranes into hybrid materials. Nat. Commun. *9*, 1521. https://doi.org/10.1038/s41467-018-02905-w.

71. Parolini, L., Mognetti, B.M., Kotar, J., Eiser, E., Cicuta, P., and Di Michele, L. (2015). Volume and porosity thermal regulation in lipid mesophases by coupling mobile ligands to soft membranes. Nat. Commun. *6*, 5948. https://doi.org/10.1038/ncomms6948.

72. Parolini, L., Kotar, J., Di Michele, L., and Mognetti, B.M. (2016). Controlling self-assembly kinetics of DNA-functionalized liposomes using toehold exchange mechanism. ACS Nano *10*, 2392–2398. https://doi.org/10.1021/acsnano.5b07201.

73. Mognetti, B.M., Cicuta, P., and Di Michele, L. (2019). Programmable interactions with biomimetic DNA linkers at fluid membranes and interfaces. Rep. Prog. Phys. *82*, 116601. https://doi.org/10.1088/1361-6633/ab37ca.

74. Julin, S., Nonappa, Shen, B., Linko, V., and Kostiainen, M.A. (2021). DNA-Origami-Templated Growth of Multilamellar Lipid Assemblies. Angew. Chem. Int. Ed. Engl. *60*, 827–833. https://doi.org/10.1002/ANIE.202006044.

75. Bolognesi, G., Friddin, M.S., Salehi-Reyhani, A., Barlow, N.E., Brooks, N.J., Ces, O., and Elani, Y. (2018). Sculpting and fusing biomimetic vesicle networks using optical tweezers. Nat. Commun. *9*, 1882. https://doi.org/10.1038/s41467-018-04282-w.

76. Tahir, M.A., Guven, Z.P., Arriaga, L.R., Tinao, B., Yang, Y.S.S., Bekdemir, A., Martin, J.T., Bhanji, A.N., Irvine, D., Stellacci, F., et al. (2020). Calcium-triggered fusion of lipid membranes is enabled by amphiphilic nanoparticles. Proc. Natl. Acad. Sci. USA *117*, 18470–18476. https://doi.org/10.1073/pnas.1902597117.

77. Filonov, G.S., Moon, J.D., Svensen, N., and Jaffrey, S.R. (2014). Broccoli: rapid selection of an RNA mimic of green fluorescent protein by fluorescence-based selection and directed evolution. J. Am. Chem. Soc. *136*, 16299–16308. https://doi.org/10.1021/ja508478x.

78. Tabor, S. (1990). Expression using the T7 RNA polymerase/promoter system. Curr. Protoc. Mol. Biol. *11*, 16.2.1–16.2.11. https://doi.org/10.1002/0471142727.MB1602S11.

79. Tschurikow, X., Gadzekpo, A., Tran, M.P., Chatterjee, R., Sobucki, M., Zaburdaev, V., Göpfrich, K., and Hilbert, L. (2023). Amphiphiles formed from synthetic DNA-nanomotifs mimic the stepwise dispersal of transcriptional clusters in the cell nucleus. Nano Lett. *23*, 7815–7824. https://doi.org/10.1021/ACS.NANOLETT.3C01301.

80. Nkanga, C.I., Ortega-Rivera, O.A., Shin, M.D., Moreno-Gonzalez, M.A., and Steinmetz, N.F. (2022). Injectable slow-release hydrogel formulation of a plant virus-based COVID-19 vaccine candidate. Biomacromolecules *23*, 1812–1825. https://doi.org/10.1021/acs.biomac.2c00112.

81. Luiz, M.T., Dutra, J.A.P., Tofani, L.B., de Araújo, J.T.C., Di Filippo, L.D., Marchetti, J.M., and Chorilli, M. (2022). Targeted liposomes: A nonviral gene delivery system for cancer therapy. Pharmaceutics *14*, 821. https://doi.org/10.3390/pharmaceutics14040821.

82. Jaekel, A., Stegemann, P., and Saccà, B. (2019). Manipulating enzymes properties with DNA nanostructures. Molecules *24*, 3694. https://doi.org/10.3390/molecules24203694.

83. Kimna, C., and Lieleg, O. (2019). Engineering an orchestrated release avalanche from hydrogels using DNA-nanotechnology. J. Control. Release *304*, 19–28. https://doi.org/10.1016/j.jconrel.2019.04.028.

84. Aumiller, W.M., Pir Cakmak, F., Davis, B.W., and Keating, C.D. (2016). RNA-based coacervates as a model for membraneless organelles: formation, properties, and interfacial liposome assembly. Langmuir *32*, 10042–10053. https://doi.org/10.1021/acs.langmuir.6b02499.

85. Pir Cakmak, F., Grigas, A.T., and Keating, C.D. (2019). Lipid vesicle-coated complex coacervates. Langmuir *35*, 7830–7840. https://doi.org/10.1021/acs.langmuir.9b00213.